Letters to ESEX

Landslide distribution and size in response to Quaternary fault activity: the Peloritani Range, NE Sicily, Italy

Francesco Bucci, Michele Santangelo, Mauro Cardinali, Federica Fiorucci and Fausto Guzzetti*
Consiglio Nazionale delle Ricerche, Istituto di Ricerca per la Protezione Idrogeologica, via Madonna Alta 126, I-06128 Perugia, Italy

*Correspondence to: Fausto Guzzetti, Consiglio Nazionale delle Ricerche, Istituto di Ricerca per la Protezione Idrogeologica, via Madonna Alta 126, I-06128 Perugia, Italy. E-mail: F.Guzzetti@irpi.cnr.it

Earth Surface Processes and Landforms

ABSTRACT: Landslides contribute to dismantle active mountain ranges and faults control the location of landslides. Yet, evidence of the long-term, regional dependency of landslides on active faults is limited. Previous studies focused on the transient effects of earthquakes on slope stability in compressive and transcurrent regimes. Here we show that in the Peloritani range, NE Sicily, Italy, one of the fastest uplifting areas in the Mediterranean, a clear geographical association exists between large bedrock landslides and active normal faults of the Messina Straits graben. By interpreting aerial photographs, we mapped 1590 landslides and sackungs and 626 fault elements and their facets in a 300 km^2 area in the eastern part of the range. We used the new landslide and fault information, in combination with prior geological and seismic information, to investigate the association between bedrock landslides and faults. We find that the distribution and abundance of landslides is related to the presence of large active normal faults, and matches the pattern of the local historical seismicity. Landslide material is more abundant along the East Peloritani Fault System where the long-term activity of the faults, measured by the average yearly geological moment rate, is larger than in the West Peloritani Fault System where landslides are less abundant. Along the fault systems landslide material concentrates where the cumulated fault throws are largest. We conclude that large landslides and their cumulated volume are sensitive to local rates of tectonic deformation, and discriminate the deformation of the single fault segments that dissect the Peloritani range. Our findings are a direct test of landscape evolution models that predict higher rates of landslide activity near active faults. Our work opens up the possibility of exploiting accurate landslide and fault maps, in combination with geological and seismic information, to characterize the long-term seismic history of poorly instrumented active regions. © 2015 The Authors Earth Surface Processes and Landforms Published by John Wiley & Sons Ltd

KEYWORDS: landslides; faults; topography; Peloritani range

Introduction

Landslides contribute to dismantle active mountain belts (Burbank et al., 1996; Larsen et al., 2010), and faults control the location and abundance of landslides caused by seismic and meteorological triggers (Guzzetti et al., 1996; Scheingross et al., 2013). Landscape evolution models predict higher rates of landslide erosion near faults (Densmore et al., 1997; Chen et al., 2014). However empirical evidence of the long-term, regional dependency of landslides on active faults remains scarce. Here, we investigate the role of active normal faults in controlling the distribution and size of landslides in the Peloritani range, one of the fastest uplifting areas in the Mediterranean region (Doglioni et al., 2012). By integrating new and existing geomorphological and geological information on the location and size of normal faults and landslides, we observe the association between landslides, recent active normal faults and historical earthquakes, and we investigate the role of the active faults in controlling the size, geographical distribution and clustering of landslides in the active range.

Study Area

We study an area in the Peloritani range, NE Sicily, Italy, where the Messina Straits graben cuts compressive structures of the Calabria-Peloritani Arc, built in the Tertiary in response to the convergence of the African and the European plates (Figure 1 (**A**)). In the range, Variscan metamorphic rocks are interposed tectonically between Mesozoic meta-sediments and chaotic Tertiary covers. The contractional architecture was modified by normal faults related to the opening of the Messina Straits (Bonini et al., 2011). The range underwent important uplift in the Quaternary, with an average rate of
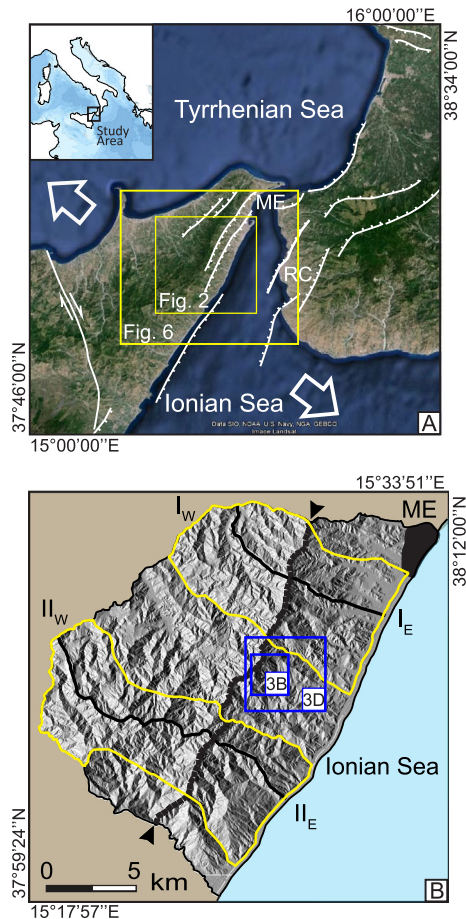
Figure 1. Location map. (A) Simplified tectonic sketch of the Messina Strait, NE Sicily and S Calabria, Italy. (B) Map of the study area showing morphology (shades of grey), sub-areas (yellow lines) and profiles (black lines) used in the study. ME, Messina. RC, Reggio Calabria. I and II show traces of profiles in Figure 5. Blue rectangles show locations of Figure 3B and 3D.

1.0–1.5 mm yr^{-1} (Antonioli et al., 2006). Recent faults (Catalano et al., 2008), deeply incised rivers, and earthquakes (Rovida et al., 2011) demonstrate that the range is active.

In our 300 km^2 study area terrain is mountainous with elevation ranging from sea level to 1250 m. A ridge oriented NNE-SSW separates the area in two sub-areas facing the Ionian Sea to the SE, and the Tyrrhenian Sea to the NW (Figure 2(**B**)). Ephemeral streams draining into the Ionian Sea are shorter and steeper than those draining into the Tyrrhenian Sea. Metamorphic and sedimentary rocks, Paleozoic to Recent in age, crop out in the area (Carbone et al., 2008), where mass movements caused by rainfall and earthquakes are abundant (Figure 2).

Materials and Methods

Through the visual interpretation of two sets of aerial photographs and limited field checks, we prepared a map showing mass movements (Cruden and Varnes, 1996), sackungs (Ambrosi and Crosta, 2006), normal faults and their facets in the Peloritani range (Figure 2). A geological map of the Messina Straits at 1:50 000 scale (APAT, 2008), and the review of prior geological and geomorphological studies (Ghisetti, 1992; Giunta et al., 2000; Carbone et al., 2008; Arisico et al., 2010; Goswami et al., 2012, 2011; De Guidi and Scudero, 2013), aided the interpretation of the aerial photographs.
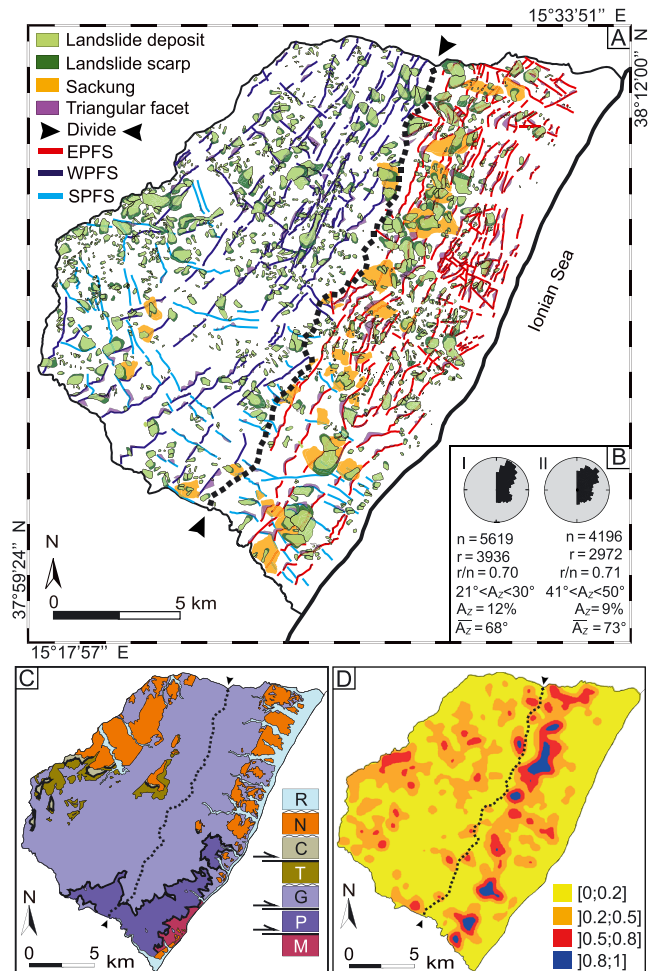

Figure 2. (A) Map of landslides, fault facets and faults. EPFS, East Peloritani Fault System. WPFS, West Peloritani Fault System. SPFS, South Peloritani Fault System. (B) Rose diagrams show strike of faults (I) identified through the interpretation of aerial photographs (this study) and (II) shown in the geological map of APAT (2008). *n* number of unit-length (100 m) fault segments, r resultant length of fault segments, r/n average resultant length of fault segments, A_Z most frequent fault azimuth value, A_Z% percentage of n with A_Z, $\overline{A_Z}$ mean azimuth value. (C) Simplified geological map. R, recent alluvial and beach sediments; N, Neogene continental and marine sediments; T, Tertiary flysch deposits; C, Cretaceous to Tertiary varicoloured clays; M, Mesozoic marine and continental meta-sediments; G, Palaeozoic high-grade paragneiss; P, Palaeozoic low-grade phyllites. (D) Map of density of landslide area A_L obtained through kernel density estimation using a 20 × 20 m raster version of the landslide inventory map shown in (A).

Aerial photographs interpretation

We interpreted black and white stereoscopic aerial photographs flown in 1955 and 2005. The old photographs were taken at a 1:33 000 nominal scale, when the extent and density of the forests were reduced compared with 2005, and significant urbanization and human modification of the landscape had not started. This facilitated the recognition of large mass movements and sackungs, including features that were subdued, partially dismantled by erosion and other failures. In the old photographs, fault lines appeared distinct and continuous, and were simple to identify. However, photographic quality of the old images was not homogenous, limiting the systematic detection and mapping of small features. The 2005 photographs were taken at a 1:28 000 nominal scale, and were of better quality than the old images. For these reasons the recent photographs allowed for a more

accurate mapping of small features, and were instrumental for mapping failures occured after 1955.

The information on mass movements and sackungs, normal faults, and facets was drawn manually on transparent plastic sheets placed over the photographs, and then transferred in a GIS using a semi-automatic procedure designed to reduce mapping errors (Santangelo et al., 2015). We estimated the mapping errors associated with the inventory to be less than 20%, on average, with small features exhibiting larger errors than the larger features. The errors are typical of landslide inventory maps (Guzzetti et al., 2012), and do not affect the interpretations. Figure 3 exemplifies the detail of our mapping, and the relationships between mass movements and sackungs, and between normal faults and their facets.

Landslides

Mass movements, including slides, flows, slide earth-flows, debris flows, rock falls, topples and complex/composite failures (Cruden and Varnes, 1996), were classified as deep-seated or shallow, with the crown area mapped separately from the deposit for the deep-seated failures (Figure 3(A), (B)). The distinction was not made for shallow failures. The deep-seated failures involved the bedrock, and most of the shallow landslides involved the soil or the weathered bedrock. We acknowledge that separation between shallow and deep-seated failures was heuristic and locally uncertain. The inventory also showed sackungs (Ambrosi and Crosta, 2006) that were mapped considering upslope dipping scarps, trenches, and duplicated ridges in the crest or in the upper part of the slopes (Figure 3(A), (B)).

In this paper, we use the term 'landslide' to encompass all mass movements and sackungs. Our inventory consists of 1590 landslides (Figure 2(A)) for which we obtained the area A_L (in m^2) in a GIS in the range $1.07 \times 10^2 < A_L < 1.34 \times 10^6$ m^2, the volume V_L (in m^3) from A_L using the general relationship $V_L = 0.074 \times A_L^{1.450}$ proposed by Guzzetti et al. (2009), and the average thickness, $D_L = V_L / A_L = 0.074 \times A_L^{1.450}/A_L$ (in m) (Table I). To evaluate the uncertainty associated to the estimation of V_L from A_L, we repeated the calculations using the relationships proposed by Larsen et al. (2010) for bedrock and for shallow landslides. Use of different relationships resulted in differences that do not affect the interpretation (Table I).

We do not have information on the age of the landslides. Based on their morphological appearance (McCalpin, 1984), the height of the slopes where large landslides were mapped, and the Holocene estimated uplift rates in the study area (1.4–2.4 mm/yr, Antonioli et al., 2006), we hypothesize that the majority of the landslides occurred in the last 10–20 kyr. However, we cannot exclude that some of the largest landslides are older.

Faults and facets

Interpretation of the old aerial photographs, aided by the analysis of the geological map (APAT, 2008), allowed mapping 626 fault strands in the length range $1.03 \times 10^2 < L_F < 3.68 \times 10^3$ m (Figure 2(A)). Geomorphological alignments, anomalies in the drainage network, and knick points were analysed, and considered evidence of recent faulting (Figure 3(C), (D)). Anomalies and knick points produced by landslides and local lithological changes were excluded from the analysis. Thrusts are present in the west and south parts of the area (Figure 2(C)), but are

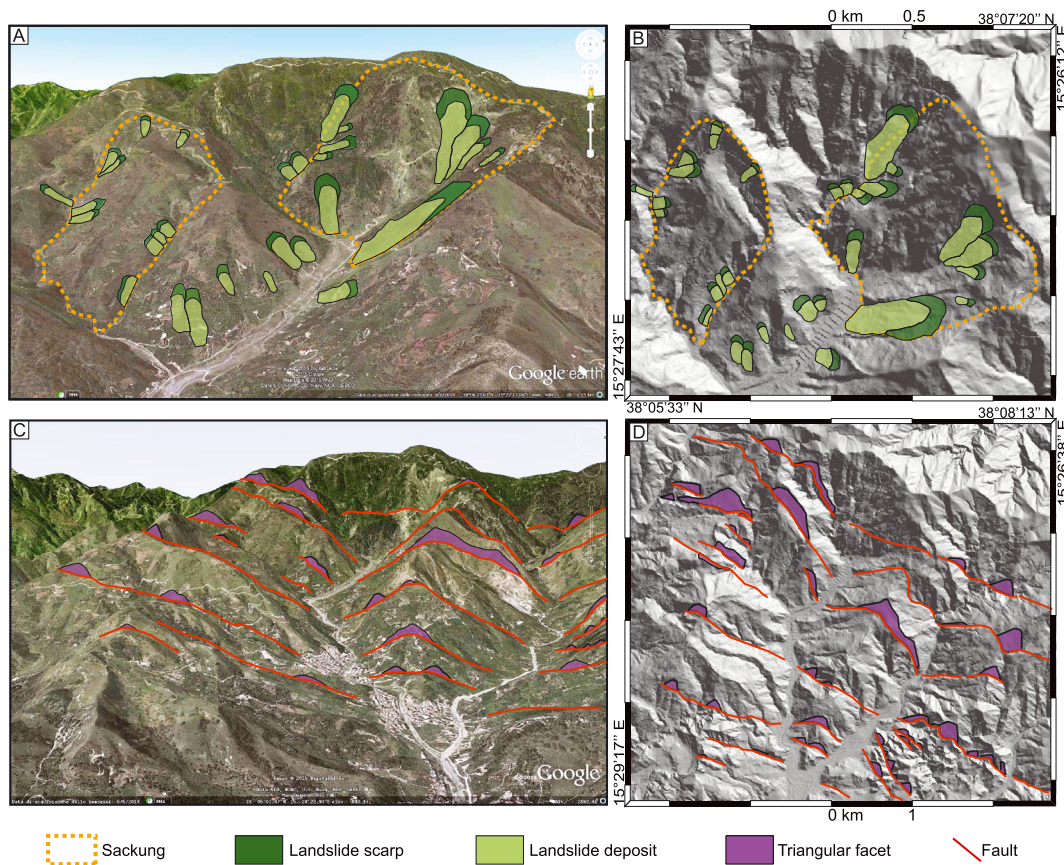| Sackung | Landslide scarp | Landslide deposit | Triangular facet | Fault |

Figure 3. Examples of typical (A, B) landslides (dark green is source area, light green is deposit) and sackungs (dotted orange line), and (C, D) faults (red line) and fault facets (violet area), in the study area. (A) and (C) are 3D views prepared using Google Earth (accessed November 2015) and (B) and (D) are corresponding maps, in 2D. Location of the two areas is given in Figure 1(B).

Table I. Statistics of landslide size in the study area. Landslide area, A_L (m^2) measured in the GIS. Landslide volume, V_L (m^3) computed using (I) the general relationship $V_L = 0.074 \times A_L^{1.450}$ proposed by Guzzetti *et al.* (2009), (II) the relationship for bedrock landslides $V_L = 0.146 \times A_L^{1.35}$ proposed by Larsen *et al.* (2010), for landslides in the range $1.07 \times 10^2 < A_L < 1.33 \times 10^6$, and (III) the relationship for shallow landslides $V_L = 0.146 \times A_L^{1.145}$ proposed by Larsen *et al.* (2010) for landslides in the range $1.35 \times 10^2 < A_L < 2.44 \times 10^5$. Average landslide thickness is computed as $D_L = V_L / A_L = 0.146 \times A_L^{1.35} / A_L$ for I, II, III, and as $D_L = (0.05 +/-0.02) \times A_L^{0.5}$ (Hovius *et al.*, 1997) for IV, using A_L and V_L from (I)

	A_L			V_L			D_L		
	Min	Max	Total	Min	Max	Total	Min	Max	Mean
I	1.07×10^2	1.33×10^6	6.88×10^7	0.67×10^2	0.56×10^8	1.29×10^9	0.6	42.1	6.7
II	1.07×10^2	1.33×10^6	6.64×10^7	0.80×10^2	0.27×10^8	0.72×10^9	0.8	20.3	5.0
III	1.35×10^2	2.44×10^5	2.36×10^6	0.40×10^2	0.22×10^6	0.14×10^7	0.3	0.9	0.5
IV							0.5	57.0	7.7

not shown in Figure 2**(A)** that considers only normal faults related to the opening of the Messina Straits graben (Bonini *et al.*, 2011).

Visual interpretation of the old photographs also allowed mapping 730 facets in the footwall of the normal faults, with area in the range $1.72 \times 10^2 < A_{TF} < 1.26 \times 10^5$ m^2 (Figure 2**(A)** Figure 3**(C), (D)**). Given the geological and morphological complexity of the area, not all the facets were well defined, and simple to identify. We acknowledge that this has introduced uncertainty in the analysis. Because facets are steep, we corrected their planimetric area measured in the GIS by the local terrain slope computed from a 2 × 2 m LiDAR DEM. To evaluate the quality of the fault map, we compared statistics of the strike of the faults in our map and in the geological map of the Messina Straits (APAT, 2008). Results revealed a good agreement between the fault strike statistics in the two maps (Figure 2**(B)**).

Fault throws

We used the LiDAR DEM to draw WNW-ESE cross-strike topographic profiles, and to measure the throw, T_F of the faults. Along the profiles we identified breaks in slope in correspondence to the mapped faults, and we measured visually in a GIS the height of the bedrock escarpments. We excluded topographic breaks caused by local lithological anomalies or landslides. We assumed that the height of the escarpment along the fault was a measure of the throw (Ganas *et al.*, 2005), and we measured T_F along the profiles. The assumption holds where high-angle normal faults sculpt the landscape (Jackson and Leeder 1994; Axen *et al.*, 1999; Ganas *et al.*, 2005; Bucci *et al.*, 2013). This is the case of the Peloritani range, where faults are steep (>70°) on the surface (Giunta *et al.*, 2000).

The measured throws are lower estimates of the vertical fault displacements, because (i) the depth to bedrock in the hanging wall was unknown, (ii) erosion may have lowered the uplifted footwall block, (iii) a sedimentary wedge of an unknown thickness may have deposited on the down dropped fault block covering it partially or totally (Tsoudoulos *et al.*, 2008), and (iv) the fault motion may not have been exactly vertical. We note a good agreement between our throws and measurements obtained from geological cross-sections using the base of the units shown in the cross-sections (Carbone *et al.*, 2008), with most differences in the range −21% to +25%, and negative (positive) differences for large (small) throws (**Table** II). We attribute the latter to uncertainties in the measurements obtained from the geological cross-sections, at 1:50 000 scale.

Results

In the study area, 5.2% of the largest landslides cover 50% of the total landslide area A_{LT}, and 1.8% of the largest failures

Table II. Comparison of throws T_F for faults shown in Figure 5. EPFS, East Peloritani Fault System. WPFS, West Peloritani Fault System. (A) T_F measurements obtained in this study. (B) T_F measurements obtained from geological cross sections (APAT, 2008). (C) Difference between A and B. (D) Maximum T_F along throw – distance profiles. (E) Maximum T_F from published displacement/length ratios (Ghisetti, 1992). (F) Difference between D and E

	A (m)	B (m)	C (%)	D (m)	E (m)	F (%)
EPFS						
F1	50	40	+20%	50	40	+20%
F2	250	500	−50%	250	225	+10%
F3	120	125	−4%	120	140	−14%
F4	230	250	−8%	230	245	−7%
F5	100	100	0%	100	110	−9%
F6	70			70	60	+14%
F7	190			190	165	+13%
F8	170	200	−15%	170	195	−13%
F9	65	50	+23%	65	60	+8%
F10	180			180	165	+8%
F11	80	70	+12%	200	195	+3%
WPFS						
F12	70	70	0%	150	140	+7%
F13	70			70	60	+14%
F14	150			150	115	+23%
F15	60	60	0%	140	195	−28%
F16	130	160	−18%	130	165	−21%
F17	80	80	0%	100	110	−9%
F18	90	110	−18%	140	140	0%
F19	40	35	+12%	70	60	+14%
F20	90	190	−58%	90	110	−18%
F21	120			120	85	+28%
F22	120	150	−20%	120	85	+28%
F23	150			150	165	−9%
F24	80			80	60	+25%
F25	100			100	85	+15%

account for 50% the total landslide volume, V_{LT} (Figure 3**(A)**). This is typical of tectonically active landscapes (Guzzetti *et al.*, 2008). Given that the large and very large failures are deep-seated, we conclude that primarily bedrock landslides generate the landslide material in the study area. Although the distribution of the main rock types is nearly symmetrical across the main divide (Figure 2**(C)**), the landslide inventory map (Figure 2**(A)**) reveals that A_{LT} concentrates to the E of the divide along a narrow NNE-SSW girdle (Figure 2**(D)**). The asymmetry is confirmed by the average thickness of the large landslides ($D_L > 10$ m, 20% of total) that is larger to the E of the main divide ($D_L = 17$ m) than to the W ($D_L = 13$ m) (Figure 4**(B)**).

In the study area, the size of the landslides increases with increasing relative relief (Figure 5). The size of the fault facets, a proxy for the size of the throw of the associated faults (Strak *et al.*, 2011), also increases with increasing relief. To quantify the evidence, we calculated the relative relief for the study
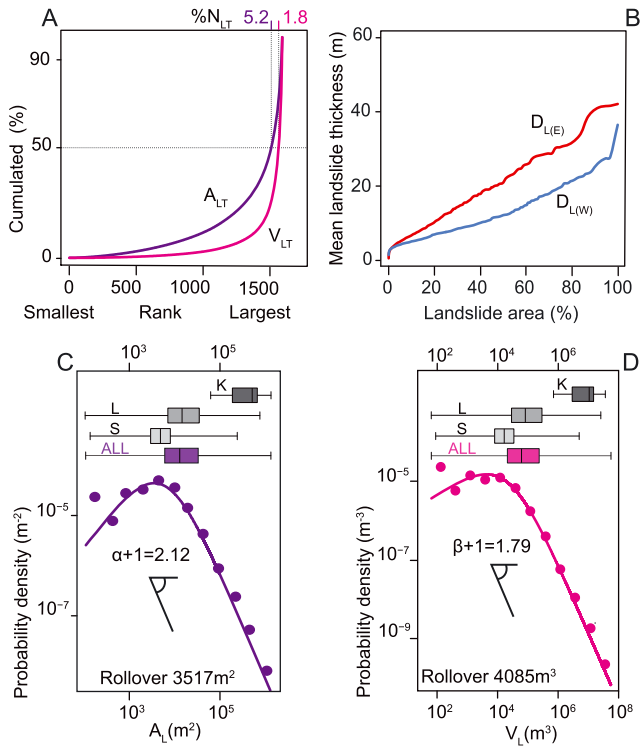
Figure 4. (A) Proportion of cumulated landslide area A_{LT} and cumulated landslide volume V_{LT}, ranked from smallest (left) to largest (right) landslide. (B) Average landslide thickness, D_L (m) for the E (red) and the W (blue) areas across the main divide. (C) Probability density of landslide area, $p(A_L)$ (all landslides considered). (D) Probability density of landslide volume, $p(V_L)$ (all landslides considered). Dots show kernel density estimates and coloured lines best-fit models. In (C) and (D) box plots show distribution of sackungs (K), shallow landslides (S), deep-seated landslides (L), and all landslides (including sackungs) (ALL).
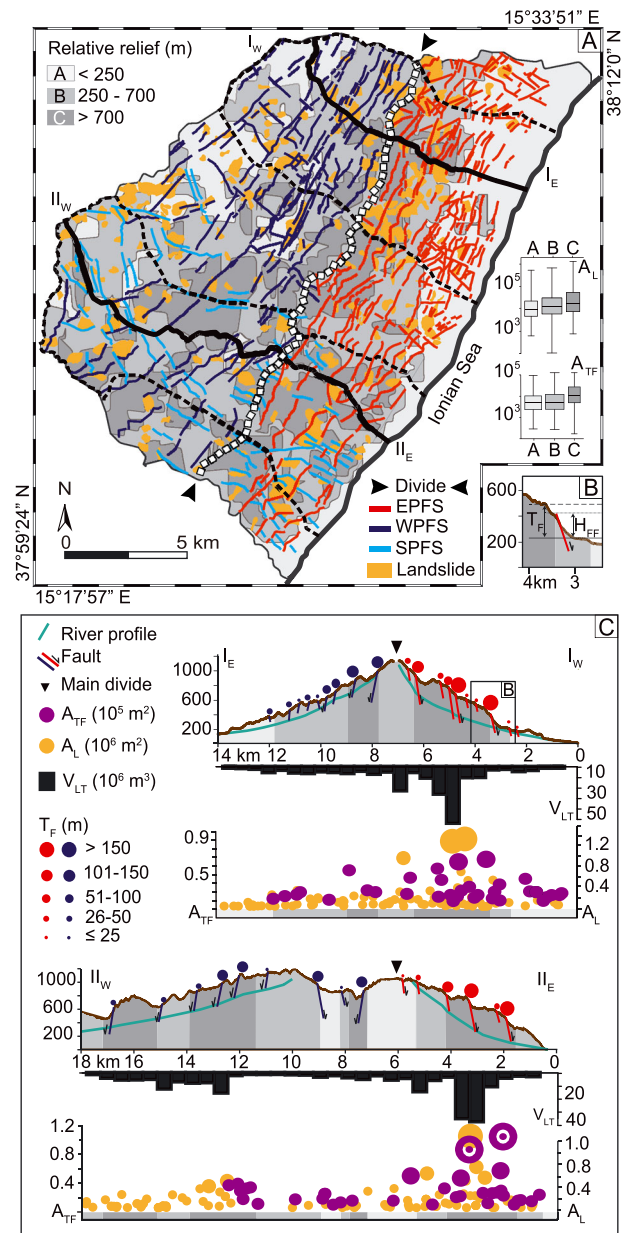

Figure 5. (A) Map of faults, facets, landslides, and relative relief. EPFS, East Peloritani Fault System. WPFS, West Peloritani Fault System. SPFS South Peloritani Fault System. Black thick lines show traces and dashed lines are boundaries of sub-areas (yellow polygons in Figure 1(**B**)) for the profiles. Box plots (in logarithmic coordinates) show distribution of A_L and A_{TF} in three classes of relative relief, and reveal that median values of A_L and A_{TF} increase with increasing relative relief. (B) Sketch illustrates the difference between fault throw T_F and maximum height of fault facet H_{FF} for the same fault. (C) Profiles I and II show association between relative relief, size of throws, total landslide volume V_{LT}, landslide area A_L, and area of facets A_{TF}.

area using a 20 × 20 m DEM obtained by downgrading the 2 × 2 m LiDAR DEM. For each cell in the coarse DEM, we calculated relative relief as the largest difference in elevation in a 45 × 45 cell kernel moved across the DEM. The size of the kernel was selected to capture general topographic variations rather than local topographic features. The box plots in Figure 5(A) (in log scale) confirm that the size of the landslides and of the facets increases with terrain relief.

We grouped the single fault strands into main faults (Figure 2(**A**)), and noticed that the NNE-SSW faults arrange in two systems (Figure 5 and Figure 6): the West Peloritani Fault System (WPFS) encompassing 14 faults dipping chiefly towards WNW to the west of the main divide, and the East Peloritani Fault System (EPFS) encompassing 11 faults dipping chiefly towards ESE to the east of the same divide. A third fault system, the South Peloritani Fault System (SPFS), includes 26 NW-SE trending faults in the southern part of the range, with no clear age relationships with the EPFS or the WPFS (Giunta *et al.*, 2000).

For each fault in the WPFS and EPFS we measured the fault length, L_F (in m) in a GIS (**Table** III), and we assessed the average yearly geological moment rate, M_G/τ a measure of the contribution of the fault to the long-term deformation (Ghisetti, 1992). For the purpose, we used the relationship $M_G/\tau = v \times \mu \times A_F$ proposed by Ghisetti (1992) for faults in the Messina Straits area. In the relationship, τ is the age of the fault (yr), v is the minimum slip rate (mm yr^{-1}), μ is the shear modulus (3×10^{10} N m^{-2}), and $A_F = L_F^2$ is the area of the fault plane (m^2). To bracket minimum and maximum values for M_G/τ, we used the limited information on the faults age available in the literature (Bonini *et al.*, 2011; Ghisetti, 1992), and

we set τ_{min} = 0.8 Myr and τ_{max} = 1.5 Myr (**Table** II). Results revealed a long-term average yearly geological moment rate for the EPFS 1.7 to 1.9 times larger than the rate for the WPFS, with the larger (smaller) value indicative of a higher (lower) degree of activity of the fault systems.

For each fault in the WPFS and EPFS, we selected the tallest facet and we used the height of the facet, H_{FF} (Figure 5(**B**)) to estimate the vertical slip rate of the fault, S_V using the empirical relationship log S_V = (0.00248 × H_{FF}) − 0.938 proposed by dePolo and Anderson (2000 (**Table** III). Considering the known variation of the relationship around the central tendency, we calculated minimum and maximum values for the slip rates. The minimum slip rates are, on average, twice the largest slip
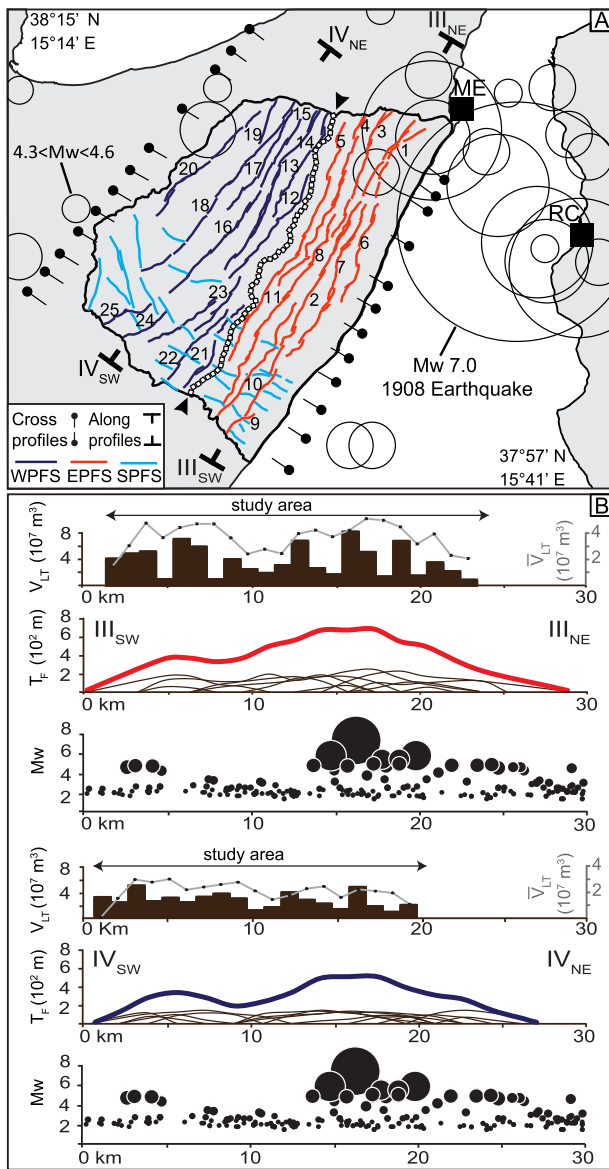
Figure 6. (A) Map of faults pertaining to the East Peloritani Fault System (EPFS, 1–11), the West Peloritani Fault System (WPFS, 12–26) (**Table** I and **Table** II), and the South Peloritani Fault System (SPFS, un-numbered). Circles show epicentre and magnitude of $M_W > 4.3$ earthquakes. ME, Messina; RC, Reggio Calabria. (B) Fault throw – distance profiles. Bars show total landslide volume V_{LT}, grey lines with black dots show total landslide volume averaged in a 3 km window $\overline{V}_{LT}$, thin black lines show throw of single faults and coloured (red, blue) lines show cumulated throw T_{FT} for all the faults. Dots show location and magnitude of $M_W > 2.0$ earthquakes in the period 1310–2006 (Valensise and Pantosti, 1992; Rovida *et al.*, 2011).

rates obtained using $\tau_{min} = 0.8$ Myr (Ghisetti, 1992; Bonini *et al.*, 2011), with larger differences for small faults and negligible differences for large faults.

We further constructed along-strike (NNE–SSW) throw-distance profiles to measure the cumulated throw for the faults in the EPFS and the WPFS (Figure 6). For the purpose, we used equally spaced cross-strike profiles drawn along the faults (Roberts and Michetti, 2004; Papanikolaou and Roberts, 2007), and for each fault we cumulated the throw along the profiles selecting faults longer than 3 km, crossed by at least three cross-strike profiles, and with $T_F > 50$ m. We found a good agreement between our maximum cumulated throws, T_{FT} and estimates obtained using the empirical relationship $T_F = cL_F^{1.2}$ proposed by Ghisetti (1992), where $c = 0.0025$ measures the unit length fault displacement (Walsch *et al.*,

2002; Kim and Sanderson, 2005) (**Table** III). We further note that our point T_F measurements are in agreement with measurements obtained from geological cross sections for the same faults at about the same locations (Carbone *et al.*, 2008), and that the maximum T_F measurements match values obtained from fault-displacement/fault-length ratios (Kim and Sanderson, 2005) (**Table** II).

We attempted an independent and indirect estimation of the age of the faults in the EPFS and WPFS. For each fault we divided T_F by the minimum slip rate for the fault obtained using the approach proposed by dePolo and Anderson (2000). Results indicate fault ages in the range 0.7–0.3 Myr (**Table** II), in good agreement with the estimates given by Ghisetti (1992) for some of the same faults in the Messina Straits. The result confirms that the mapped faults are recent in age, and have controlled the evolution of the landscape, increasing topographic relief and contributing to landsliding, in the past 0.3–0.7 Myr.

To study the dependence of (large) landslides on faults, we analysed the geographic distribution of landslides size and fault throw across and along the Peloritani range. Figure 5(**C**) shows cross-strike (WNW–ESE) profiles illustrative of the north and the south parts of the study area. We drew the profiles along the divides to avoid intersecting landslide escarpments that would have altered the T_F measurements. Inspection of Figure 5 (**C**) confirms the geographical association between large faults, areas with high local relief, and the presence of large landslides in the north and south parts of our study area. The larger difference in elevation between the valley bottoms (blue lines below topographic profiles in Figure 5(**C**)) and the adjacent divides along the east side of the range, reveals the deeper cutting of the streams that drain into the Ionian Sea, closer to the centre of the graben, and where intense tectonically driven uplift was active for the last 125 kyr (Antonioli *et al.*, 2006).

Figure 6 shows cumulated throw-distance profiles drawn along the strike of the WPFS and the EPFS, with the largest V_{LT} occurring where the T_{FT} is also largest, and both metrics reducing significantly towards the north end of the fault systems. The association is stronger along the EPFS, characterized by larger T_{FT} and larger values of the geological moment rate, M_G/τ (Figure 6(**B**)). Along the EPFS, large values of M_G/τ measured by the larger T_F, coincide with large V_{LT}, confirming the association between active faults and large landslides. A second peak in the cumulated displacement T_{FT}, also associated to a peak of V_{LT}, is present in the sothern part of the area where the EPFS interferes with the SPFS. The short faults of the SPFS have increased relative relief and rock fracturing, favouring the formation of large landslides. The evidence suggests that V_{LT} is not related to a specific fault system (e.g. EPFS), but it depends on the presence of active faults, arranged in one or more fault systems. Overall, we explain the geographical association between large landslides and large faults observing that the large faults have increased the topographic relief, amplifying locally the geometric conditions that favour the formation of landslides. Large faults have also disturbed larger volumes of rocks, and the mechanical weakening of the rocks has favoured the formation of larger landslides. This is in agreement with findings in the Umbria-Marche Apennines, central Italy (Guzzetti and Cardinali, 1991), in the Northern Apennines, Italy (Carlini *et al.*, 2016), along the San Andreas fault, California (Scheingross *et al.*, 2013), and along the continental slope off the cost of Israel (Katz *et al.*, 2015).

Our study area bounds to the northwest the Messina Straits graben, an area characterized by historical seismicity (Valensise and Pantosti, 1992; Rovida *et al.*, 2011). The seismic record lists moderate to strong earthquakes in the period 1310–2006 in or near the Messina Straits. The strongest earthquakes occurred a few kilometres offshore the Ionian coast, with moderate earthquakes onshore. Several Mw > 4.3

© 2015 The Authors Earth Surface Processes and Landforms Published by John Wiley & Sons Ltd

Earth Surf. Process. Landforms, Vol. **41**, 711–720 (2016)

Table III. Metrics for faults shown in Figure 5. EPFS, East Peloritani Fault System. WPFS, West Peloritani Fault System. SPFS, South Peloritani Fault System. L_F, fault length (m). $A_F = L_F^2$ fault area ($m^2 \times 10^6$). T_F, fault throw (m). τ, age of the fault set to $\tau_{min} = 0.8$ Myr and $\tau_{max} = 1.5$ Myr based on information from Ghisetti (1992) and Bonini et al. (2011). u_{min}, minimum fault slip rate (m $yr^{-1} \times 10^{-3}$). M_G, total geological moment (N m$\times 10^{20}$). M_G/τ, average yearly geological moment rate (N m $yr^{-1} \times 10^{13}$). H_{FF}, maximum height of facet along the fault measured from the fault trace to the top of the facet (m). log $S_V = 0.00248 H_{FF} - 0.938$ from dePolo and Anderson (2000) measures the vertical slip rate. S_{Vmin} and S_{Vmax} are the minimum and maximum estimated slip rates (m $yr^{-1} \times 10^{-3}$). T, age of the fault (Myr) calculated in this study using the minimum slip rate S_{Vmin} for the fault. C, cumulated value. GC, cumulated value for all faults in the EPFS and WPFS

	L_F	A_F	H_{FF}	T_F	τ	u_{min}	M_G	M_G/τ	log S_V	S_{Vmax}	S_{Vmin}	T
EPFS												
F1	3.0	9.0	30	50	1.5-0.8	0.03-0.06	0.12	0.81-1.62	−0.86	0.72	0.25	0.20
F2	13.5	182.3	205	250	1.5-0.8	0.17-0.31	13.94	92.97-169.53	−0.43	1.11	0.38	0.66
F3	9.0	81.0	100	120	1.5-0.8	0.08-0.15	2.92	19.44-36.45	−0.69	0.85	0.30	0.41
F4	14.5	210.3	195	230	1.5-0.8	0.15-0.28	14.19	94.63-176.65	−0.45	1.08	0.37	0.62
F5	7.5	56.3	110	100	1.5-0.8	0.07-0.12	1.77	11.82-20.26	−0.67	0.87	0.30	0.33
F6	4.5	20.3	50	70	1.5-0.8	0.05-0.08	0.46	3.04-4.87	−0.81	0.75	0.26	0.27
F7	10.5	110.3	135	190	1.5-0.8	0.13-0.23	6.45	43.00-76.10	−0.60	0.93	0.32	0.59
F8	12.0	144.0	150	170	1.5-0.8	0.11-0.21	7.13	47.52-90.72	−0.57	0.97	0.33	0.52
F9	4.5	20.3	65	65	1.5-0.8	0.04-0.08	0.36	2.43-4.87	−0.78	0.78	0.27	0.24
F10	10.5	110.3	140	180	1.5-0.8	0.12-0.22	5.96	39.71-72.80	−0.59	0.94	0.33	0.56
F11	12.0	144.0	150	200	1.5-0.8	0.13-0.25	8.42	56.16-108.00	−0.57	0.97	0.33	0.60
C	98.5	1079.1	13300	1575								
WPFS												
F12	9.0	81.0	120	150	1.5-0.8	0.10-0.18	3.64	24.30-43.74	−0.64	0.90	0.31	0.48
F13	4.5	20.3	80	70	1.5-0.8	0.05-0.08	0.46	3.04-4.87	−0.74	0.81	0.28	0.25
F14	7.5	56.3	130	150	1.5-0.8	0.10-0.18	2.53	16.89-30.40	−0.62	0.92	0.32	0.48
F15	12.0	144.0	100	140	1.5-0.8	0.09-0.17	5.83	38.88-73.44	−0.69	0.85	0.30	0.48
F16	10.5	110.3	130	130	1.5-0.8	0.09-0.17	4.47	29.78-56.25	−0.62	0.92	0.32	0.40
F17	7.5	56.3	80	100	1.5-0.8	0.07-0.12	1.77	11.82-20.26	−0.74	0.81	0.28	0.36
F18	9.0	81.0	110	140	1.5-0.8	0.09-0.17	3.28	21.87-41.31	−0.67	0.87	0.30	0.47
F19	4.5	20.3	60	70	1.5-0.8	0.05-0.08	0.46	3.04-4.87	−0.79	0.77	0.27	0.26
F20	7.5	56.3	85	90	1.5-0.8	0.06-0.11	1.52	10.13-18.58	−0.73	0.82	0.28	0.32
F21	6.0	36.0	115	120	1.5-0.8	0.08-0.15	1.30	8.64-16.20	−0.65	0.88	0.31	0.39
F22	6.0	36.0	95	120	1.5-0.8	0.08-0.15	1.30	8.64-16.20	−0.70	0.84	0.29	0.41
F23	10.5	110.3	120	150	1.5-0.8	0.10-0.18	4.96	33.09-59.56	−0.64	0.90	0.31	0.48
F24	4.5	20.3	85	80	1.5-0.8	0.05-0.08	0.46	3.04-4.87	−0.73	0.82	0.28	0.29
F25	6.0	36.0	90	100	1.5-0.8	0.07-0.12	1.13	7.56-12.96	−0.71	0.83	0.29	0.34
C	105.0	864.4	1400	1610								
GC	203.5	1943.5	2700	3185								

earthquakes occurred at less than 10 km from the part of the study area facing the Straits (Figure 6), which has therefore experienced multiple shaking events; and earthquake shaking is a known trigger of landslides (Keefer, 2013). Although we do not know the triggers of the single landslides in our inventory, we note the geographical concurrence of large landslides and high seismicity along the east side of the Peloritani range. To investigate the evidence, we plot all $M_W > 2.0$ earthquakes within 10 km from the perimeter of the study area along the EPFS and WPFS profiles (Figure 6(**B**)), and we find that the distribution of V_{LT} obeys the geographical pattern of the seismicity, with a cluster of fifteen $M_W > 4.5$ earthquakes coinciding with the largest peak of V_{LT}. We further observe that only six moderate (4.3 < M_W < 4.9) earthquakes have occurred W of the main divide, and their geographical distribution is not associated to peaks in V_{LT}. Figure 6(**B**) shows that in the areas that have experienced multiple, moderate to strong shaking events seismicity and landslide patterns are spatially associated.

The abundance of large landslides near major Quaternary faults suggests that ground acceleration, possibly enhanced by local amplification phenomena, contributed to the initiation and development of large landslides in the study area (Sleep, 2011). The 28 December 1908, 7.1 M_W Messina earthquake, the strongest historical earthquake in the region, triggered numerous rock falls, rock slides, slides, and later spreads, most of which were within 40 km from the epicentre (Comerci et al., 2015). In our mapping we did not recognize signs of the 1908 landslides, probably because evidence of the co-seismic failures was obliterated by urbanization and land-cover changes.

However, Comerci et al. (2015) have argued that some of the 1908 co-seismic failures were partial reactivations of pre-existing landslides. Thus, it is possible that at least some of the 1908 co-seismic landslides occurred inside larger and older landslides shown in our inventory.

Discussion

In the eastern part of the Peloritani range a clear association exists between large landslides and normal faults. This is demonstrated by the geographical distribution of A_{LT} and V_{LT} that increase almost systematically where the throws of the normal faults are higher, and where local relief is large. Large throws, high relative relief, and steep terrain are the results of the long-term activity of numerous normal faults in the area resulting from the opening of the Messina Straits (Bonini et al., 2011; Doglioni et al., 2012). Large cumulated landslide volumes are also associated to moderate-to-strong (>4.3 M_w) earthquakes (Figure 6). Despite lack of exact dates for the faults and the landslides, the empirical evidence suggests a relationship between the short-term (0 to 1 kyr) perturbation of topography produced by historical earthquakes, the medium-term (1 to 100 kyr) morphological instability caused by regional tectonic uplift, deep river incision and bedrock landslides, and the long-term (100 kyr to 1 Myr) effects of active normal faults on the evolving landscape. We conclude that the geographical clustering of large volumes of landslide materials in the East Peloritani range is indicative of long-term active

tectonics, and a direct result of local bedrock uplift induced by active normal faulting.

Assuming that the historical earthquake record (Valensise and Pantosti, 1992) is a good proxy for the long-term (Quaternary) seismicity in the Messina Straits, we infer that the long-term seismicity was responsible for the overall reduction of the rock strength (Molnar *et al.*, 2007; Sleep, 2011) and the related mobilization of large volumes of materials by large bedrock landslides, not necessarily all co-seismically induced (Katz *et al.*, 2014). We expect rock weakening caused by repeated earthquakes to be more intense (and effective) along active faults that exhibit large throws, where the deformation is largest. At these locations, ground motion caused by earthquakes may also be enhanced by topographic and structural amplification.

In our study area, the cumulated landslide materials are most abundant along the EPFS, where topographic and structural seismic amplification is expected to be large (Figure 6(**B**)). This is evidence that large slope movements and their cumulated volumes are sensitive to local rates of tectonic deformation, and discriminate the cumulated deformation of individual fault segments inside the complex fault systems dissecting the Peloritani range. Inspection of landslide maps for the east side of the Messina Straits, in Calabria, confirms the association between large landslides and normal faults (Goswami *et al.*, 2012). Since there is nothing peculiar or unique in the type of the landslides and the normal faults in our area, or in the Messina Straits, we hypothesize that the same may occur in similar extensional settings in the Mediterranean (e.g. the Gulf of Corinth, Tsoudoulos *et al.*, 2008), and elsewhere (e.g. the Ethiopian Rift, Abebe *et al.*, 2010).

Previous studies focused on compressive tectonic settings revealed that the regional pattern of co-seismic landslides depends on earthquake shaking and contains information about the earthquake source mechanism (Meunier *et al.*, 2013). A correlation between the geographical pattern of landslide erosion and co-seismic deformation was documented in the central range of Taiwan (Dadson *et al.*, 2003), a tropical subduction zone where landscape-lowering rates from earthquake-triggered landslides are large (Jibson, 2013). Our work extends the dependency between bedrock landslides (not only seismically induced) on active tectonics to an extensional setting, and to significantly longer time scales, from historical to Quaternary. Since many shallow landslides in our study area occur inside or in the proximity of larger deep-seated landslides, the dependency holds, at least partly, also for shallow landslides.

Conclusions

Analysis of the results of an accurate mapping of landslides, normal faults and their facets in the eastern Peloritani range, northeast Sicily, Italy, and of geological and seismic information for the same area, allows for the following specific and general considerations.

In the study area, one of the fastest uplifting areas in the Mediterranean (Doglioni *et al.*, 2012), large bedrock landslides produce the majority of the landslide material (Figure 2 and Figure 4). This is typical of tectonically active landscapes (Guzzetti *et al.*, 2008). Our mapping revealed a clear geographical association between large bedrock landslides and recent active normal faults related to the opening of the Messina Straits (Bonini *et al.*, 2011; Doglioni *et al.*, 2012). The faults, 0.2 to 0.7 Myr in age (**Table** III), are characterized by large throws and large local relief (Figure 5). In the area, the distribution of the landslide material also matches the

geographical pattern of the local historical seismicity (Valensise and Pantosti, 1992; Rovida *et al.*, 2011) (Figure 6).

Our analysis revealed that landslide material is more abundant along the EPFS (Figure 2) where the long-term activity of the fault system, measured by the average yearly geological moment rate (Ghisetti, 1992), is significantly larger than in the WPFS, where landslides are less abundant (Figure 5). In the two fault systems landslide material concentrates where the cumulated fault throws are largest (Figure 6(**B**)). We conclude that the asymmetry in the distribution of the landslide material (Figure 2(**D**)) and the association between large landslides, large active faults and earthquakes (Figure 5 and Figure 6) is the result of the activity of normal faults related to the opening of the Messina Straits (Bonini *et al.*, 2011; Doglioni *et al.*, 2012). The faults have increased topographic relief and have disturbed large volumes of rocks, amplifying locally the conditions that favour slope instability and the formation of large landslides. We hypothesize that the same occurs in similar extensional tectonic settings (Tsoudoulos *et al.*, 2008; Abebe *et al.*, 2010).

We further note that the distribution and abundance of landslide material in the study area is not related to a specific fault system (e.g. the EPFS), but to the presence of the recent active normal faults arranged in one or more fault systems (Figure 5). We conclude that large landslides and their cumulated volume are sensitive to local rates of tectonic deformation, and discriminate the cumulated deformation of individual fault segments inside the complex fault systems dissecting the Peloritani range (Figure 2). This finding is a direct empirical test of landscape evolution models that predict higher rates of landslide activity near active faults to balance the higher rates of rock uplift (Densmore *et al.*, 1997; Chen *et al.*, 2014).

We end by emphasizing that accurate geomorphological landslide and fault maps (Guzzetti *et al.*, 2012), in combination with geological and seismic information, can contribute to characterize the long-term seismic history of poorly instrumented active regions (Meunier *et al.*, 2013), to investigate the medium- to long-term seismicity of an area, and to extend or supplement information on historical earthquakes, benefiting seismic hazard assessments.

Appendix

Variables and acronyms used in text.

Variable	Description	Unit
c	Constant related to material mechanical properties	-
n	Number of unit-length (100 m) fault segments	-
r	Resultant length of fault segments	-
r/n	Mean resultant length of fault segments	-
A_F	Area of the fault	m^2
A_L	Area of a slope movement	m^2
A_{LT}	Total area of slope movements	m^2
A_{TF}	Area of triangular facet	m^2
A_Z	Most frequent fault azimuth value	deg
$\overline{A_Z}$	Average fault azimuth value	deg
D_L	Average landslide thickness	m
H_{FF}	Maximum height of fault facet	m
L_F	Fault length	km
M_G	Geological moment	N m
M_W	Earthquake magnitude (moment magnitude scale)	-

(*Continues*)

Appendix: (Continued)

Variable	Description	Unit
N_{LT}	Total number of landslides	#
S_V	Vertical fault slip rate, estimated in this study	mm yr^{-1}
T	Age of a fault, estimated in this study	Myr
T_F	Fault throw	m
T_{FT}	Cumulated fault throw	m
V_L	Volume of a slope movement	m^3
V_{LT}	Total volume of slope movements	m^3
$\overline{V}_{LT}$	Total landslide volume averaged in a 3 km window	m^3
μ	Shear modulus of the material	N m^{-2}
ν	Fault slip rate, from literature	mm yr^{-1}
ς	Fault area	km^2
τ	Age of a fault, from literature	Myr
Acronym		
EPFS	East Peloritani Fault System	
SPFS	South Peloritani Fault System	
WPFS	West Peloritani Fault System	

References

Abebe B, Dramis F, Fubelli G, Umer M, Asrat A. 2010. Landslides in the Ethiopian highlands and the Rift margins. *Journal of African Earth Sciences* **56**: 131–8. DOI:10.1016/j.jafrearsci.2009.06.006.

Ambrosi C, Crosta GB. 2006. Large sackung along major tectonic features in the Central Italian Alps. *Engineering Geology* **83**: 183–200. DOI:10.1016/j.enggeo.2005.06.031.

Antonioli F, Ferranti L, Lambeck K, Kershaw S, Verrubbi V, Dai PG. 2006. Late Pleistocene to Holocene record of changing uplift rates in southern Calabria and northeastern Sicily (southern Italy, Central Mediterranean Sea). *Tectonophysics* **422**: 23–40. DOI:10.1016/j.tecto.2006.05.003.

APAT. 2008. Carta Geologica d'Italia alla scala 1:50.000, Foglio 601 Messina – Reggio Calabria. S.EL.CA, Firenze.

Arisico G, Arnone G, Favara R, Nigro F, Perricone M, Renda P, Mondeeello C. 2010. Integrated neotectonic and morphometric analysis of northern Sicily. *Bollettino Società Geologica Italiana* **125**: 221–44.

Axen GJ, Fletcher JM, Cowgill E, Murphy M, Kapp P, MacMillan I, Ramos-Velázquez E, Aranda-Gómez J. 1999. Range-front fault scarps of the Sierra El Mayor, Baja California: Formed above an active low-angle normal fault? *Geology* **27**: 247–50. DOI:10.1130/0091-7613 (1999)027<0247:rffsot>2.3.co;2.

Bonini L, Di Bucci D, Toscani G, Seno S, Valensise G. 2011. Reconciling deep seismogenic and shallow active faults through analogue modelling: the case of the Messina Straits (southern Italy). *Journal Geological Society* **168**: 191–9. DOI:10.1144/0016-76492010-055.

Bucci F, Cardinali M, Guzzetti F. 2013. Structural geomorphology active faulting and slope deformations in the epicentre area of the MW 7.0 1857, Southern Italy earthquake. *Physics and Chemistry of the Earth* **63**: 12–24. DOI:10.1016/j.pce.2013.04.005.

Burbank DW, Leland J, Fielding EJ, Anderson RS, Brozovic N, Reid MR, Duncan C. 1996. Bedrock incision, rock uplift and threshold hillslopes in the northwestern Himalayas. *Nature* **379**: 505–10. DOI:10.1038/379505a0.

Carbone S, Messina A, Lentini F, Barbano MS, Grasso D, Di Stefano A, Ferrara V, Somma R. 2008. Note Illustrative della Carta Geologica d'Italia alla Scala 1:50.000. Foglio 601 Messina-Reggio di Calabria. Servizio Geologico d'Italia, APAT-Regione Siciliana, 1, 1–179. S.EL. CA., Firenze.

Carlini M, Chelli A, Vescovi P, Artoni A, Clemenzi L, Tellini C, Torelli L. 2016. Tectonic control on the development and distribution of large landslides in the Northern Apennines (Italy). *Geomorphology* **253**(C): 425–437. DOI:10.1016/j.geomorph.2015.10.028.

Catalano S, De Guidi G, Romagnoli G, Torrisi S, Tortorici G, Tortorici L. 2008. Active faulting and seismicity along the Siculo–Calabrian Rift Zone (Southern Italy). *Tectonophysics* **453**: 177–92. DOI:10.1016/j. tecto.2007.05.008.

Chen A, Darbon J, Morel J-M. 2014. Landscape evolution models: A review of their fundamental equations. *Geomorphology* **219**(C): 68–86. DOI:10.1016/j.geomorph.2014.04.037.

Comerci V, Vittori E, Blumetti AM, Brustia E, Di Manna P, Guerrieri L, Lucarini M, Serva L. 2015. Environmental effects of the December 28, 1908, Southern Calabria–Messina (Southern Italy) earthquake. *Natural Hazards* **76**: 1849–91. DOI:10.1007/s11069-014-1573-x.

Cruden DM, Varnes DJ. 1996. Landslide types and processes. In *Landslides, Investigation and Mitigation*, AK T, RL S (eds), Transportation Research Board Special Report 247. National Academy Press: Washington DC; 36–75.

Dadson SJ, Hovious N, Chen H, Dade WB, Hsieh ML, Willett SD, Hu JC, Horng MJ, Chen MC, Stark CP, Lague D, Lin JC. 2003. Links between erosion, runoff variability and seismicity in the Taiwan orogeny. *Nature* **426**: 648–51. DOI:10.1038/nature02150.

De Guidi G, Scudero S. 2013. Landslide susceptibility assessment in the Peloritani Mts. (Sicily, Italy) and clues for tectonic control of relief processes. *Natural Hazards and Earth System Sciences* **13**: 949–63. DOI:10.5194/nhess-13-949-2013.

Densmore AL, Anderson RS, McAdoo BG, Ellis MA. 1997. Hillslope evolution by bedrock landslides. *Science* **275**(5298): 369–72. DOI:10.1126/science.275.5298.369.

dePolo CM, Anderson JG. 2000. Estimating the slip rates of normal faults in the Great Basin, USA. *Basin Research* **12**: 227–40. DOI:10.1111/j.1365-2117.2000.00131.x.

Doglioni C, Ligi M, Scrocca D, Bigi S, Bortoluzzi G, Carminati E, Cuffaro M, D'Oriano F, Forleo V, Muccini F, Riguzzi F. 2012. The tectonic puzzle of the Messina area (Southern Italy): insights from new seismic reflection data. *Scientific Reports* **2**: 970. DOI:10.1038/ srep00970.

Ganas A, Pavlides S, Karastathis V. 2005. DEM-based morphometry of range-front escarpments in Attica, central Greece, and its relation to fault slip rates. *Geomorphology* **65**: 301–19.

Ghisetti F 1992. Fault parameters in the Messina Strait (Southern Italy) and relations with the seismogenic source. *Tectonophysics* **210**: 117–33. DOI:10.1016/0040-1951(92)90131-o.

Giunta G, Nigro F, Renda P, Giorgianni A. 2000. The Sicilian-Maghrebides Tyrrhenian Margin: a neotectonic evolutionary model. *Bollettino Società Geologica Italiana* **119**: 553–65.

Goswami R, Brocklehurst SH, Mitchell NC. 2012. Erosion of a tectonically uplifting coastal landscape, NE Sicily, Italy. *Geomorphology* **171–172**: 114–26. DOI:10.1016/j.geomorph.2012.05.011.

Goswami R, Mitchell NC, Brocklehurst SH. 2011. Distribution and causes of landslides in eastern Peloritani of NE Sicily and western Aspromonte of SW Calabria, Italy. *Geomorphology* **132**: 111–22. DOI:10.1016/j.geomorph.2011.04.036.

Guzzetti F, Ardizzone F, Cardinali M, Galli M, Reichenbach P, Rossi M. 2008. Distribution of landslides in the Upper Tiber River basin, central Italy. *Geomorphology* **96**(1–2): 105–122. DOI: 10.1016/j. geomorph.2007.07.015.

Guzzetti F, Ardizzone F, Cardinali M, Rossi M, Valigi D. 2009. Landslide volumes and landslide mobilization rates in Umbria, Central Italy. *Earth and Planetary Science Letters* **279**: 222–9. DOI:10.1016/j.epsl.2009.01.005.

Guzzetti F, Cardinali M. 1991. Debris-flow phenomena in the Central Apennines of Italy. *Terra Nova* **3**: 619–27. DOI:10.1111/j.1365-3121.1991.tb00204.x.

Guzzetti F, Cardinali M, Reichenbach P. 1996. The influence of structural setting and lithology on landslide type and pattern. *Environmental & Engineering Geoscience* **2**(4): 531–55. DOI:10.2113/ gseegeosci.ii.4.531.

Guzzetti F, Mondini AC, Cardinali M, Fiorucci F, Santangelo M, Chang K-T. 2012. Landslide inventory maps: New tools for an old problem. *Earth-Science Reviews* **112**: 42–66. DOI:10.1016/j. earscirev.2012.02.001.

Hovius N, Stark CP, Allen PA. 1997. Sediment flux from a mountain belt derived by landslide mapping. *Geology* **25**: 231–4. DOI:10.1130/0091-7613(1997)025<0231:sffamb>2.3.co;2.

Jackson JA, Leeder M. 1994. Drainage systems and the development of normal faults: an example from Pleasant Valley, Nevada. *Journal of Structural Geology* **16**: 1041–59. DOI:10.1016/0191-8141(94)90051-5.

Jibson RW. 2013. Mass-Movement Causes: Earthquakes. In *Treatise on Geomorphology, 7, Mountain and Hillslope Geomorphology*, Shroder J, Marston RA, Stoffel M (eds). Academic Press: San Diego; 223–229. DOI: 10.1016/B978-0-12-374739-6.00169-X.

Katz O, Morgan JK, Aharonov E, Dugan B. 2014. Controls on the size and geometry of landslides: insights from discrete element numerical simulations. *Geomorphology* **220**(C): 104–13. DOI:10.1016/j.geomorph.2014.05.021.

Katz O, Reuven E, Aharonov E. 2015. Submarine landslides and fault scarps along the eastern Mediterranean Israeli continental-slope. *Marine Geology* **369**(C): 100–15. DOI:10.1016/j.margeo.2015.08.006.

Keefer DK. 2013. Landslides Generated by Earthquakes: Immediate and Long-Term Effects. In *Treatise on Geomorphology, 5, Tectonic Geomorphology*, Shroder J, Owen LA (eds). Academic Press: San Diego; 250–266. DOI: 10.1016/B978-0-12-374739-6.00091-9.

Kim YS, Sanderson DJ. 2005. The relationship between displacement and length of faults: a review. *Earth-Science Reviews* **68**: 317–34.

Larsen IJ, Montgomery DR, Korup O. 2010. Landslide erosion controlled by hillslope material. *Nature Geoscience* **3**(4): 247–51. DOI:10.1038/NGEO776.

McCalpin JP. 1984. Preliminary age classification of landslides for inventory mapping. Proceedings 21st Engineering Geology and Soil Engineering Symposium, 99–111.

Meunier P, Uchida T, Hovius N. 2013. Landslide patterns reveal the sources of large earthquakes. *Earth and Planetary Science Letters* **363**: 27–33. DOI:10.1016/j.epsl.2012.12.018.

Molnar P, Anderson RS, Anderson SP. 2007. Tectonics, fracturing of rock, and erosion. *Journal of Geophysical Research* **112**: F03014. DOI:10.1029/2005JF000433.

Papanikolaou DI, Roberts GP. 2007. Geometry, kinematics and deformation rates along the active normal fault system in the Southern Apennines: implications for fault growth. *Journal of Structural Geology* **29**: 166–88. DOI:10.1016/j.jsg.2006.07.009.

Roberts GR, Michetti AM. 2004. Spatial and temporal variations in growth rates along active normal fault systems: an example from The Lazio–Abruzzo Apennines, central Italy. *Journal of Structural Geology* **26**: 339–76. DOI:10.1016/s0191-8141(03)00103-2.

Rovida A, Camassi R, Gasperini P, Stucchi M. 2011. *CPTI11, versione 2011, Catalogo Parametrico dei Terremoti Italiani*. Milano, Bologna, http://emidius.mi.ingv.it/CPTI. DOI: 10.6092/INGV.IT-CPTI11.

Santangelo M, Marchesini I, Bucci F, Cardinali M, Fiorucci F, Guzzetti F. 2015. An approach to reduce mapping errors in the production of landslide inventory maps. *Natural Hazards and Earth System Sciences* **15**(9): 2111–26. DOI:10.5194/nhess-15-2111-2015.

Scheingross JS, Minchew BM, Mackey BH, Simons M, Lamb MP, Hensley S. 2013. Fault-zone controls on the spatial distribution of slow-moving landslides. *Geological Society of America Bulletin* **125**(3–4): 473–89. DOI:10.1130/B30719.1.

Sleep NH. 2011. Deep-seated downslope slip during strong seismic shaking. *Geochemistry Geophysics Geosystems* **12**: 1–19. DOI:10.1029/2011GC003838.

Strak V, Dominguez S, Petit C, Meyer B, Loget N. 2011. Interaction between normal fault slip and erosion on relief evolution: Insights from experimental modelling. *Tectonophysics* **513**: 1–19. DOI:10.1016/j.tecto.2011.10.005.

Tsoudoulos IM, Koukouvelas IK, Pavlides S. 2008. Tectonic geomorphology of the easternmost extension of the Gulf of Corinth (Beotia, Central Greece). *Tectonophysics* **453**: 211–32. DOI:10.1016/j.tecto.2007.06.015.

Valensise G, Pantosti D. 1992. A 125 Kyr-long geological record of seismic source repeatability: The Messina Straits (southern Italy) and the 1908 earthquake (MS 71/2). *Terra Nova* **4**: 472–83.

Walsch JJ, Nicol A, Childs C. 2002. An alternative model for the growth of faults. *Journal of Structural Geology* **24**: 1669–75.

© 2015 The Authors Earth Surface Processes and Landforms Published by John Wiley & Sons Ltd

Earth Surf. Process. Landforms, Vol. **41**, 711–720 (2016)